Astronomy & Astrophysics manuscript no. weaver
January 13, 2022
©ESO 2022

arXiv:1801.09691v2 [astro-ph.GA] 12 Jul 2018

History and destiny of an emerging early-type galaxy

New IFU insights on the major-merger remnant NGC 7252

J. Weaver[1,2], B. Husemann[2], H. Kuntschner[3], I. Martín-Navarro[4,2], F. Bournaud[5], P.-A. Duc[6,5,7], E. Emsellem[3,8], D. Krajnović[9], M. Lyubenova[3], and R. M. McDermid[10,11]

[1] SUPA, School of Physics and Astronomy, University of St Andrews, North Haugh, St Andrews KY16 9SS, UK
e-mail: jrw20@st-andrews.ac.uk
[2] Max-Planck-Institut für Astronomie, Königstuhl 17, 69117 Heidelberg, Germany
[3] European Southern Observatory, Karl-Schwarzschild-Strasse 2,85748 Garching, Germany
[4] University of California Observatories, 1156 High Street, Santa Cruz, CA 95064, USA
[5] Laboratoire AIM Paris-Saclay, CEA/IRFU/SAp, Université Paris Diderot, 91191 Gif-sur-Yvette Cedex, France
[6] Université de Strasbourg, CNRS, Observatoire Astronomique de Strasbourg, UMR 7550, 67000 Strasbourg, France
[7] Université Paris Diderot, AIM, Sorbonne Paris Cité, CEA, CNRS, 91191 Gif sur Yvette, France
[8] Observatoire de Lyon, Centre de Recherche Astrophysique de Lyon and Ecole Normale Supérieure de Lyon, Université Lyon 1, 9 Avenue Charles André, 69230 Saint-Genis Laval, France
[9] Leibniz–Institut für Astrophysik Potsdam (AIP), An der Sternwarte 16, 14482 Potsdam, Germany
[10] Department of Physics and Astronomy, Macquarie University, Sydney, NSW 2109, Australia
[11] Australian Astronomical Observatory, PO Box 915, Sydney, NSW 1670, Australia

ABSTRACT

Context. The merging of galaxies is one key aspect in our favourite hierarchical ΛCDM Universe and is an important channel leading to massive quiescent elliptical galaxies. Understanding this complex transformational process is ongoing.
Aims. We aim to study NGC 7252, which is one of the nearest major-merger galaxy remnants, observed ∼1 Gyr after the collision of presumably two gas-rich disc galaxies. It is therefore an ideal laboratory to study the processes inherent to the transformation of disc galaxies to ellipticals.
Methods. We obtained wide-field IFU spectroscopy with the VLT-VIMOS integral-field spectrograph covering the central $50'' \times 50''$ of NGC 7252 to map the stellar and ionised gas kinematics, and the distribution and conditions of the ionised gas, revealing the extent of ongoing star formation and recent star formation history.
Results. Contrary to previous studies, we find the inner gas disc not to be counter-rotating with respect to the stars. In addition, the stellar kinematics appear complex with a clear indication of a prolate-like rotation component which suggests a polar merger configuration. The ongoing star formation rate is $2.2 \pm 0.6\ M_\odot\ \mathrm{yr}^{-1}$ and implies a typical depletion time of ∼2 Gyr given the molecular gas content. Furthermore, the spatially resolved star formation history suggests a slight radial dependence, moving outwards at later times. We confirm a large AGN-ionised gas cloud previously discovered ∼5 kpc south of the nucleus, and find a higher ionisation state of the ionised gas at the galaxy centre relative to the surrounding gas disc. Although the higher ionisation towards the centre is potentially degenerate within the central star forming ring, it may be associated with a low-luminosity AGN.
Conclusions. Although NGC 7252 has been classified as post-starburst galaxy at the centre, the elliptical-like major-merger remnant still appears very active. A central kpc-scale gas disc has presumably re-formed quickly within the last 100 Myr after final coalescence. The disc features ongoing star formation, implying Gyr long timescale to reach the red sequence through gas consumption alone. While NGC 7252 is useful to probe the transformation from discs to ellipticals, it is not well-suited to study the transformation from blue to red at this point.

Key words. galaxies: individual: NGC 7252 – galaxies: elliptical and lenticular, cD – galaxies: formation – galaxies: interactions

1. Introduction

Mergers of galaxies are a natural consequence of the hierarchical build-up of large-scale structure, and emergent from our concordance Λ cold dark matter (ΛCDM) cosmological model. This model has been shown to provide a good working paradigm to describe the formation and evolution of dark matter haloes and their galaxies within (e.g. Springel et al. 2005b). In particular, the merger of two late-type (disc) galaxies has become a major scenario to assemble massive early-type (elliptical) galaxies, as shown by early numerical simulations (e.g. Hernquist & Barnes 1991; Barnes 1992). Despite the success of this scenario, we have yet to fully understand the various processes at play during major mergers, made complex by intricate baryonic physics, radiative feedback, and the hydrodynamics and chemistry of the gas.

Since the pioneering work to understand the role of hierarchical merging in the formation of early-type galaxies, numerical simulations have continued to mature due to increased resolution, implementation of more refined and extended prescriptions of baryonic physics, and larger statistical samples (e.g. Naab & Burkert 2003; Bournaud et al. 2005; Di Matteo et al. 2008; Genel et al. 2014; Vogelsberger et al. 2014a,b; Schaye et al. 2015; Tsatsi et al. 2017; Li et al. 2018). These and other inclusions now allow for quantitative predictions of various merger remnant properties. One major issue identified by the simula-

tions is that massive early-type galaxies appear too blue, due to high continuous star formation resulting from gas inflow during the merger (e.g. Hopkins et al. 2013). This has often been addressed by invoking energetic feedback from active galactic nuclei (AGN) which too are ignited following gas inflow, but subsequently expel gas from their host galaxy core and hence suppress star formation (e.g. Di Matteo et al. 2005; Springel et al. 2005a; Somerville et al. 2008). This has lead to a popular scenario in which AGN play a key role in shaping the properties of early-type galaxies during their assembly, following from a two disc major merger (e.g. Sanders et al. 1988; Hopkins et al. 2008; Schawinski et al. 2010).

Observationally, integral-field spectroscopy has provided a significant step forwards in understanding early-type galaxy formation by recovering the 2D projected internal dynamics and properties, and hence a fossil record of their formation process. Integral-field unit (IFU) surveys covering a large number of early-type galaxies, such as SAURON (de Zeeuw et al. 2002), ATLAS^{3D} (Cappellari et al. 2011), CALIFA (Sánchez et al. 2012), SAMI (Croom et al. 2012), MaNGA (Bundy et al. 2015), or the MASSIVE surveys (Ma et al. 2014), have revealed a rich variety of kinematic properties and sub-structures (e.g. Emsellem et al. 2004, 2011; Krajnović et al. 2008, 2013; Falcón-Barroso et al. 2017; Veale et al. 2017; van de Sande et al. 2017). Based on the 2D mapped kinematics, the specific angular momentum has been proposed as a metric for classifying fast and slow rotating early-type galaxies (Cappellari et al. 2007; Emsellem et al. 2011). While dedicated numerical simulations have shown that this classification does not reflect a bimodality in their merger histories (Naab et al. 2014), differences between these populations remain. Observationally, the fraction of fast to slow rotators seems to be a strong function of stellar mass (Emsellem et al. 2011; Veale et al. 2017) and fast rotators frequently show strong evidence of disc-like structures, often with increased metallicity and younger ages (Krajnović et al. 2008; Kuntschner et al. 2010). These populations also have been identified as having different star formation histories and star formation quenching timescales (Smethurst et al. 2018).

While the transformation from discs to an elliptical galaxy can be readily addressed through simulations guided mainly by gravitation, the star formation histories are related to complex baryonic physics which are difficult to fully implement. Indeed, early-type galaxies are known to show a great variety of ionised (e.g. Sarzi et al. 2006; Singh et al. 2013), atomic (e.g. Serra et al. 2012) and molecular gas content (e.g. Young et al. 2011), which can have an internal or external origin, as discussed in Davis et al. (2011), which depend on environment and merger history. This highlights the complexity in the star formation histories and associated processes responsible for transforming blue (star-forming) disc galaxies into red (quiescent) elliptical galaxies. While fast quenching of early-type galaxies has been often proposed in light of AGN feedback (e.g. Schawinski et al. 2010), inconsistent quenching timescales of several Gyr have also been observed (e.g. Weigel et al. 2017; Smethurst et al. 2018).

It is therefore still necessary to observe and characterise ongoing major mergers at various evolutionary phases in order to establish a complete picture of their transformation. Given the decreasing major merger rate towards lower redshift (e.g. Lotz et al. 2011; Rodriguez-Gomez et al. 2015), these events are particularly rare in the local Universe. This scarcity has driven detailed studies of spatially resolved nearby major mergers such as the Mice (NGC 4676; e.g. Barnes 2004; Wild et al. 2014), the Antennae (NGC 4038,NGC 4039; e.g. Whitmore et al. 2010; Ueda et al. 2012), or the Atoms-for-peace galaxy (NGC 7252; e.g. Schweizer 1982; Wang et al. 1992; Hibbard et al. 1994; Schweizer et al. 2013). While these individual galaxies are not necessarily representative of the entire population and the total parameter space concerning major mergers, they nonetheless provide important information about the transformational processes.

In this article, we focus on NGC 7252 ($z = 0.016$) aiming to uncover the history and destiny of this enigmatic merger remnant based on new wide-field optical IFU observations. The system is well studied with many ancillary observations available, providing a well-defined framework from which to interpret our new observations. Bright tidal tails are clearly visible around NGC 7252, which are rich in atomic H I gas (Hibbard et al. 1994). Numerical simulations suggest that these features are produced by a major merger of two gas-rich galaxies which rarely last longer than ~ 500 Myr (e.g. Duc & Renaud 2013) after the first passage of the galaxies. A dedicated numerical simulation of NGC 7252 has been presented by Chien & Barnes (2010) to study the star formation history during this merger. Their simulation predicts a rise in the star formation rate (SFR) when the two galaxies approached the first close passage at pericentre about ~ 620 Myr ago. Another burst in star formation is associated with the second encounter about ~ 260 Myr ago, followed by the final coalescence of the nuclei about 215 Myr ago. A prolonged star-formation episode lasting for ~ 60 Myr is predicted by the simulations without significant levels of star formation thereafter. While the stellar population at the very central galaxy core is indeed characterised by a post-starburst spectrum (Fritze-v. Alvensleben & Gerhard 1994), it is surrounded by a rotating disc of molecular (Wang et al. 1992; Ueda et al. 2014) and ionised gas (Schweizer 1982) within ~ 8" (2.4 kpc) which is still actively forming stars. The surface brightness profile of NGC 7252 has already become well-described by a $r^{1/4}$ law (e.g. Schweizer 1982; Rothberg & Joseph 2004), suggesting that NGC 7252 is close to finishing the transformational process from two disc galaxies to an elliptical galaxy.

The paper is organised as follows: in section 2 we give a brief report of the observations and data reduction. This is followed by the section 3 where we present the analysis and results which are discussed in more detail in section 4. The paper finishes with a summary and conclusion in section 5. Throughout the paper we adopt a concordance cosmological model with $H_0 = 70\,\mathrm{km\,s^{-1}Mpc^{-1}}$, $\Omega_\mathrm{m} = 0.3$, and $\Omega_\Lambda = 0.7$.

2. Observations and data reduction

We observe the central $50'' \times 50''$ of NGC 7252 with the VIsible MultiObject Spectrograph (VIMOS) instrument (Le Févre et al. 2003) using the integral-field unit (IFU) mode in October 2011 as part of programme 088.B-0224 (PI: H. Kuntschner). With the high-resolution blue grating of VIMOS we cover a wavelength range from 4130Å to 6200Å with a spectral resolution of $R \sim 2550$ over a $27'' \times 27''$ field-of-view per individual pointing. Hence, we cover the main body of NGC 7252 with four pointings that slightly overlap to always cover the centre of the galaxy as shown in Fig. 1. Each pointing is observed twice for 1500 s together with 500 s long blank sky field exposure. Three lamp flat exposures as well as one arc lamp exposure are observed as night time calibrations. Standard star observations for our setup are taken as part of the standard calibration plan.

The data reduction is performed entirely with the PyP3D data reduction package (Husemann et al. 2013) that has been developed for fibre-fed IFUs as part of the Calar Alto Large Integral Field Area survey (CALIFA, Sánchez et al. 2012). It has already

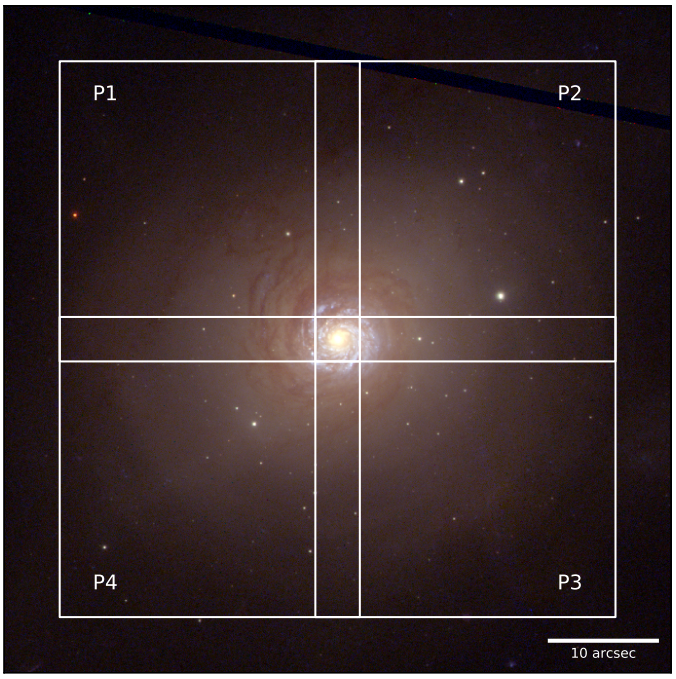


Fig. 1. Field-of-view of the four independent VIMOS pointings. A white box denotes each pointing, overlaid on a colour image of NGC 7252 taken with WFC3 aboard *Hubble* in the bands F336W, F475W and F775W (Bastian et al. 2013).

been successfully used to reduce several VIMOS IFU data sets (Husemann et al. 2014; Woo et al. 2014; Richtler et al. 2017) and we follow the same scheme here, as briefly described below.

After bias subtraction, cosmic rays are detected with PyCosmic (Husemann et al. 2013) and flagged throughout the processing. Fibres are identified in the combined lamp images and the cross-dispersion width of fibre profiles are estimated as a function of wavelength to allow for an optimal extraction (Horne 1986) of the fibre counts, even in the presence of severe cross-talk between fibres. From the arc lamp observations we determine the wavelength solution for each fibre as well as the spectral resolution which can vary significantly across the four independent spectrographs. We applied the wavelength solution to the data after extraction and adaptively smooth the data to a common spectral resolution of 3 Å, corresponding to the worst resolution found among the data sets. Fibre-to-fibre transmission differences are corrected using a fibre-flat created from the continuum lamp observations of each corresponding observing block. Flexure of the instrument is handled by measuring the shifts of sky line spots in the science data cross-dispersion and dispersion direction. Flux calibration is performed by reducing standard star observations in exactly the same way as the data from which a response function is determined by comparing the observed counts with the reference spectrum.

In post-processing we subtract the sky background as measured from the reduced blank sky field closest in time. Due to varying levels of stray light, the background is subtracted independently in each spectrograph quadrant. The effect of differential atmospheric refraction is accounted for by tracing the bright centre of the galaxy as a function of wavelength in each observation. The final datacube measuring $50'' \times 50''$ is then re-constructed from the individual flux-calibrated and sky-subtracted pointings using the drizzle algorithm (Fruchter & Hook 2002). The galaxy centre serves as the reference point to align all pointings over the entire wavelength range.

When computing absolute quantities from the resulting spectra in the IFU data, a good absolute spectrophotometric calibration is key. We check the accuracy of our absolute spectrophotometric accuracy by comparing the IFU data with the photometry of the available *Hubble* images in the F475W filter, corresponding to Sloan *g* band. Our VIMOS spectral range covers more than 90% of the effective F475W filter band. We measure $m_{\rm IFU} = 13.0\,$mag (AB) compared to $m_{\rm HST} = 12.9\,$mag (AB) within an aperture of $30''$ in diameter centred on the nuclear region of NGC 7572. Hence, we adopt a systematic photometric error of $\leq 10\%$ for all absolute quantities inferred from the VIMOS data.

3. Analysis and results

3.1. Stellar and emission line modelling

The signal-to-noise ratio (S/N) of the stellar continuum varies significantly over the VIMOS field-of-view (FoV). Thus, in order to obtain the best stellar kinematics for the entire field, spectra are co-added using the Voronoi binning algorithm (Cappellari & Copin 2003) with a target $S/N \sim 50$. This produces a total of 135 co-added spectra, with the largest bins near the edges of the field where the brightness is significantly less than at the field centre, as expected.

Continua of the 135 spectra are then fitted with PyParadise, an extended Python version of Paradise (Walcher et al. 2015). We adopt the input library of single stellar population spectra from the Medium-Resolution Isaac Newton Telescope Library of Empirical Spectra (MILES; Sánchez-Blázquez et al. 2006; Vazdekis et al. 2010; Falcón-Barroso et al. 2011). The upper panel of Fig. 2 is presented as an example, whereby the spectrum of the most central and brightest spaxel, which also corresponds to a single Voronoi bin, is fitted with the continuum model.

Emission line regions are masked during the continuum fitting and normalisation, highlighted in grey. The width of these exclusion regions allows for an emission line to remain masked despite the peculiar velocities of each bin. One may note the O I bright sky line residual around 5577 Å (observed frame), which is also excluded. Although the spectra of most Voronoi bins agree with the target continuum S/N, the spectra of the edge regions, even though heavily binned, still exhibit unacceptably low S/N which is related to limited area per bin at the edges of the VIMOS FoV. These bins are discarded for clarity. The resulting stellar radial velocity and velocity dispersion maps are shown in panels a and b of Fig. 3, respectively.

Emission lines are extracted with PyParadise after the best-fit stellar continuum model is subtracted from the initial data. Given the higher S/N in the emission lines, we repeat the stellar continuum fitting on the unbinned cube but use the previously inferred Voronoi-binned stellar kinematics field as a fixed prior. Hence, only the linear superposition of stellar-population synthesis spectral basis is performed per spaxel and the best-fitting continuum model, at fixed stellar kinematics, is subtracted after which the emission lines are fitted in the residual spectrum. An example of the emission-line modelling for this two-step fitting process is shown in the lower panel of Fig. 2 for the innermost spaxel, which also represents a single Voronoi bin given its high S/N. The emission lines are selected a priori in the rest frame and treated as Gaussian profiles. Kinematic error estimates are derived from a 30 trial bootstrapping on each spectrum. The resulting gas radial velocity and velocity dispersion maps are shown

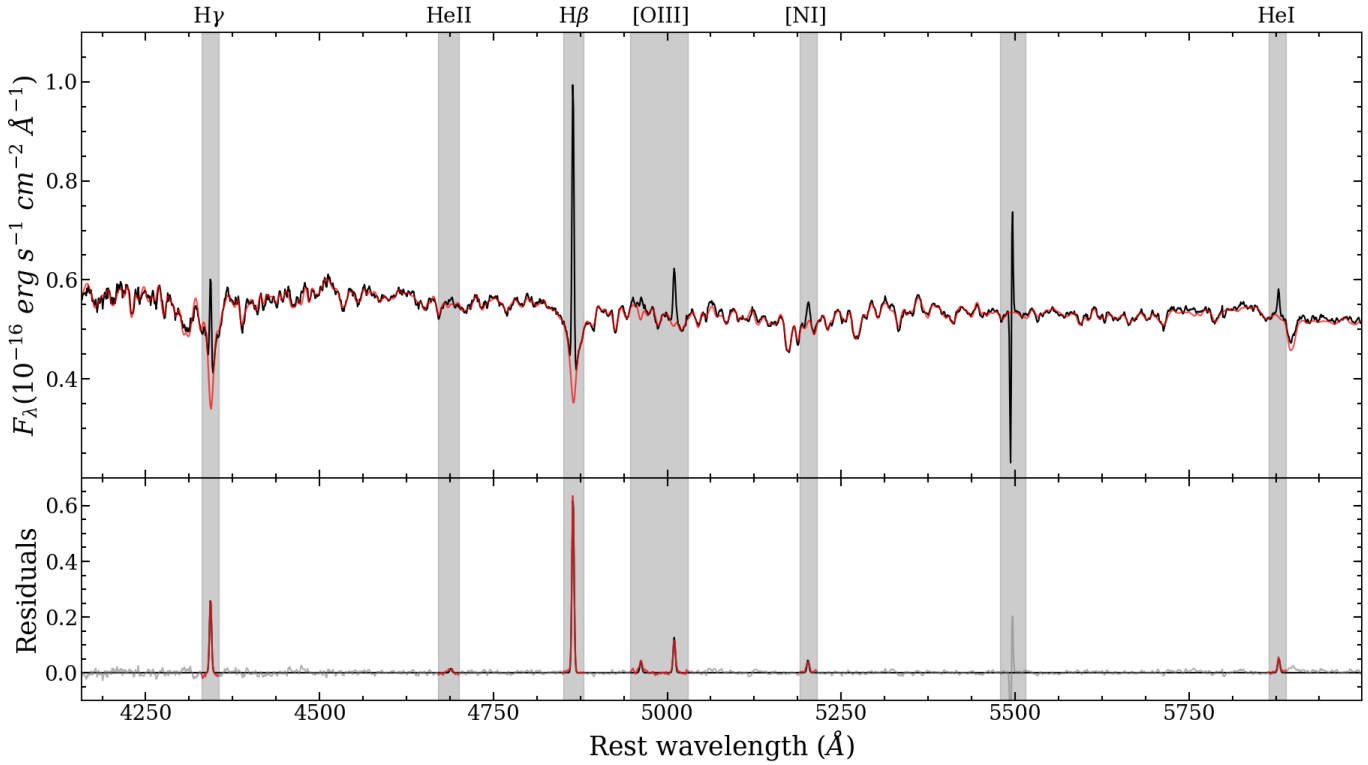


Fig. 2. Example spectral modelling of the brightest spaxel at the galaxy centre. The top panel shows the stellar continuum (black), fitted with a model spectrum (red). Regions around emission lines (grey) are omitted from the continuum fit. The bright O I sky line at 5577 Å (observed frame) is also omitted. The bottom panel shows the emission line model (red), obtained by fitting the residuals (grey) of the spaxel and continuum model. Rest-frame transformation is calculated from cosmological redshift alone ($z = 0.016$).

in panels e and f of Fig. 3. We also obtain line fluxes with PyParadise. The Hβ and [O III] λ5007 (shortly [O III] hereafter) surface brightness maps are shown in panels c and g, respectively.

As with the continua fitting, the central regions produce high S/N line detections which rapidly deteriorate towards the edges of the field. Spaxels with S/N < 3, a radial velocity error > 60 km s^{-1}, or FWHM error > 150 km s^{-1} are deemed insignificant and discarded. The pixel retention for the gas kinematic maps in panels e and f is carried over from the [O III] flux map in panel g.

3.2. Ionised gas kinematic modelling

One of the most interesting features of NGC 7252 is a central rotating gas disc (see Fig. 3 panels e and f) which exhibits a low velocity dispersion. The p–v diagram (Fig. 4 upper panel) is typical for an inclined rotating disc and we examine the disc kinematics by fitting the radial velocity map using DiskFit (Spekkens & Sellwood 2007; Sellwood & Spekkens 2015). From DiskFit, we obtain a disc kinematic position angle $PA_{gas} = -65° \pm 1°$ (counter-clockwise with respect to north, solid arrow in Fig. 3 panels (e) and (f)), an ellipticity of 0.10±0.04, and a disc inclination of 26°±5°. Our disc inclination value agrees well with the most recent findings by Ueda et al. (2014), whereby the molecular gas disc is shown to have an inclination angle of 23°±3°. However, earlier results by Schweizer (1982), obtained with slit spectra, find a conflicting inclination angle of 41°±9°.

We utilise the inclination-corrected aperture velocity measurements from DiskFit to investigate the velocity curve of the inner 6″ (2 kpc) of the disc. As shown in Fig. 4, the velocity curve flattens around 1.25 kpc to an inclination-corrected circular velocity of $v_{circ} = 229 \pm 45$km s^{-1}. The apparent decline of velocity in the outer annuli is significantly affected by higher noise and beam smearing effects at the edge of the visible gas disc. Whether the velocity curve would remain flat or really declines is therefore not possible to verify. The velocity of the inner gas disc leads to an enclosed dynamical mass of $M_{dyn}(R < 1.75\text{kpc}) = (2.1 \pm 0.9) \times 10^{10}\ M_\odot$.

In addition to the inner gas disc, we detect outer gas streams to the north-east (NE) and south-west (SW) (Fig. 3 panel e) which also appear to have a low velocity dispersion. As seen in the narrow-band imaging of Schweizer et al. (2013), these gas streams may be related to the larger gas tails which encircle the nucleus. The outer gas streams appear to have a velocity gradient nearly perpendicular to that of the inner gas disc, which initially led to the conclusion that the inner gas disc is counter-rotating with respect to the main body of the galaxy (e.g. Wang et al. 1992). However, if these gas streams are indeed related to the tidal tails this conclusion is not necessarily valid, as discussed further in section 3.3.

The significantly increased velocity dispersion of the gas disc towards the galaxy centre may be either related to shock-like ionisation as indicated by emission line diagnostics (see section 3.4), or simply caused by the beam smearing of the strong gas velocity gradient at the centre. The connection between gas excitation and velocity dispersion as commonly observed in the diffuse ionised gas phase in and around galaxies (e.g. Monreal-Ibero et al. 2010; Ho et al. 2014) is consistent with the first scenario. Indeed, it could be related to weak activity of an AGN as discussed in section 4.3. On the other hand, high central gas dispersions are also a common feature in rotating gas discs due to the observational limitation of the beam smearing. Quantifying

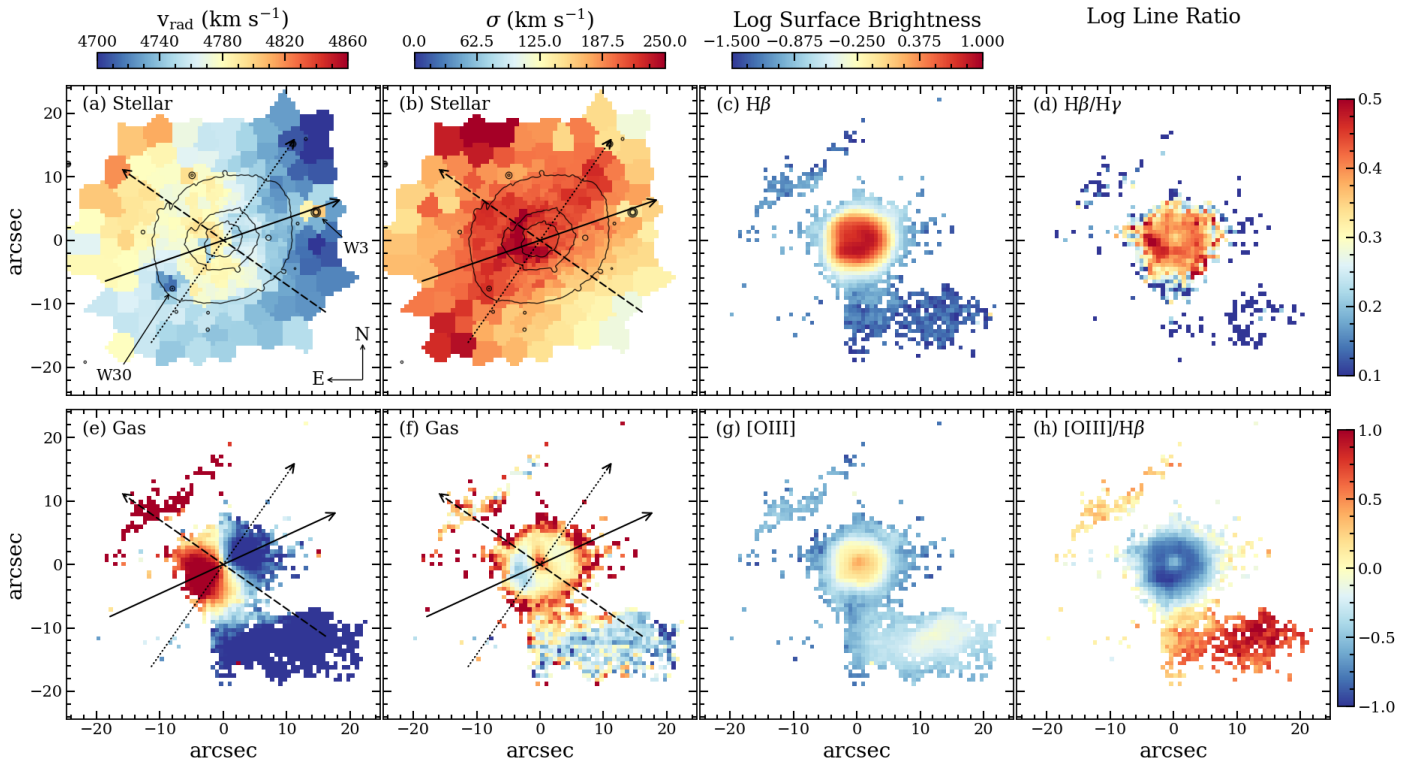


Fig. 3. Kinematic and emission line overview. The stellar maps in *panels a* and *b* are derived from kinematic measurements on 135 Voronoi co-added spectra using PyParadise. Overlaid black contours at 24, 25, and 26 mag arcsec^{-2} (AB) are constructed from smoothed F775W *Hubble* imaging (Bastian et al. 2013). The gas kinematic maps in *panels e* and *f* are derived from emission line measurements on each spaxel, excluding pixels with low S/N or high velocity and dispersion errors. Position angles are indicated by arrows. The major axis of gas and stellar kinematics agree within 6°, shown both as solid lines. The axis of the prolate-like rotation is shown as the dashed line and the photometric PA is shown by the dotted line as measured from elliptical isophotes at >15″. The gas flux maps are shown in *panels c* and *g*, in units of Log(10^{-16}erg s^{-1}cm^{-2}). The Balmer ratio map in *panel d* serves as an approximate extinction map and the variation in ionisation hardness is highlighted by the [OIII]/Hβ ratio in *panel g*.

if beam smearing alone can explain the peak in velocity dispersion with sufficient precision is not possible in this case as we lack information on the intrinsic unsmoothed line flux distribution and a model of the PSF for these observations. In reality, we expect that both effect, beam smearing and change in physical condition, contribute to the high line dispersion at the nucleus.

3.3. Stellar kinematics

The stellar radial velocity map shows a clear east-west velocity gradient with a similar position angle and rotation as the circumnuclear gas disc. This clearly suggests that the gas disc is not counter-rotating and indeed shares the same angular momentum vector as the stellar component. This rules out the gas counter-rotating with the stars as suggested by Wang et al. (1992).

Similar to the methods described in section 3.2 for the gas disc, we use DiskFit to obtain the position angle of the stellar radial velocity component PA$_{\rm stellar}$, measured over the same inner 6″ (2 kpc). This measurement yields PA$_{\rm stellar}$ = −71° ± 10° (counter-clockwise with respect to north, solid arrow in Fig. 3 panels (a) and (b)). PA$_{\rm stellar}$ is readily consistent with PA$_{\rm gas}$. We find that the inclination as derived from the stellar radial velocity map (i = 18 ± 23°) are consistent with results from the gas disc (i = 26 ± 5°), but suffer from slightly larger error bars.

To check whether NGC 7252 can be classified as a fast or slow rotator (e.g. Emsellem et al. 2007, 2011), we computed the projected specific angular momentum λ_R as described in (Emsellem et al. 2007) from the stellar velocity and velocity dispersion maps. Ancillary information on the effective radius ($R_{\rm eff}$), ellipticity (ϵ) and photometric position angle (PA$_{\rm phot}$) was obtained through ellipse isophotal fitting of the archival *Hubble* F775W and F475W images using the Python Photutils package (Bradley et al. 2017). Those measurements lead to $R_{\rm eff}$ = 4.9 ± 0.3 kpc, $\epsilon_{\rm eff}$ = 0.21 ± 0.03 and $\lambda_{R_{\rm eff}}$ = 0.17 ± 0.3 as well as PA$_{\rm phot}$ = −35° (counter-clockwise with respect to north, dotted arrow in Fig. 3). In Fig. 5, we compare our measurements with those of early-type galaxies from ATLAS$^{\rm 3D}$ as published by Emsellem et al. (2011). We find that NGC 7252 lies very close to the dividing line, with no robust way to determine its future evolution considering dynamical relaxation and stellar population ageing. Only by comparing observations with matched simulations can we obtain a good prediction, with the caveat that it is difficult and often ambiguous to connect the kinematics to the merger histories (Naab et al. 2014).

However, there is also a noticeable velocity gradient in the north-south direction, that is prolate-like rotation, which exhibits the same sense of motion as the outer gas streams, but with lower amplitude in velocity. The PA of this component is roughly 55° (counter-clockwise with respect to north, Fig. 3) as measured by connecting the highest residual velocity bins. Hence, the stars appear to be a superposition of two different kinematic structures with nearly orthogonal angular momentum vectors. Such a kinematic structure could arise from a polar galaxy merger (Tsatsi et al. 2017) or the spin angular momentum in a radial galaxy merger (Li et al. 2018). Hence, a large range of initial merger conditions can lead to prolate-like rotation (Ebrova &

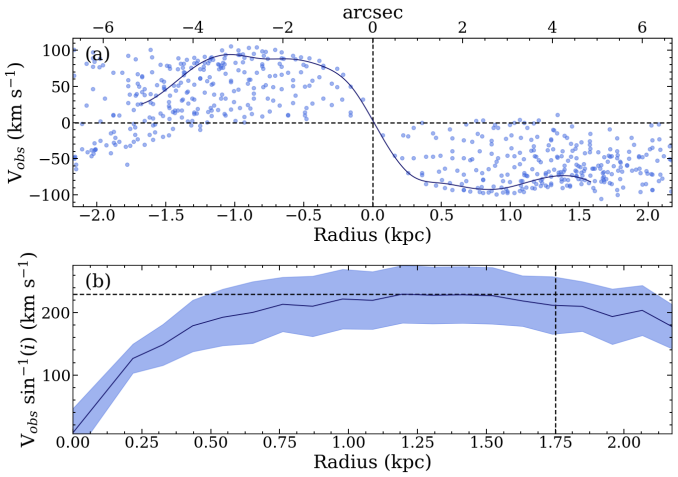


Fig. 4. Velocity pattern of the nuclear star-forming disc. *Panel a*: shows the p–v diagram of the ionised gas kinematics of all pixels within the central 2 kpc. It shows a nice rotational pattern with zero velocity along the minor axis. The velocity profile along the major axis from the DiskFit model is shown as the solid line. *Panel b*: shows the inclination-corrected velocity curve derived from aperture fittings using DiskFit. The curve flattens around 1.25 kpc from the centre of the disc, at a circular velocity of $v_{\rm circ} = 229 \pm 45$km s^{-1}. We attribute the fall off at large radii to noise. The intersecting dotted black lines indicate the point from which the dynamical mass of the disc is calculated, as discussed in the text.

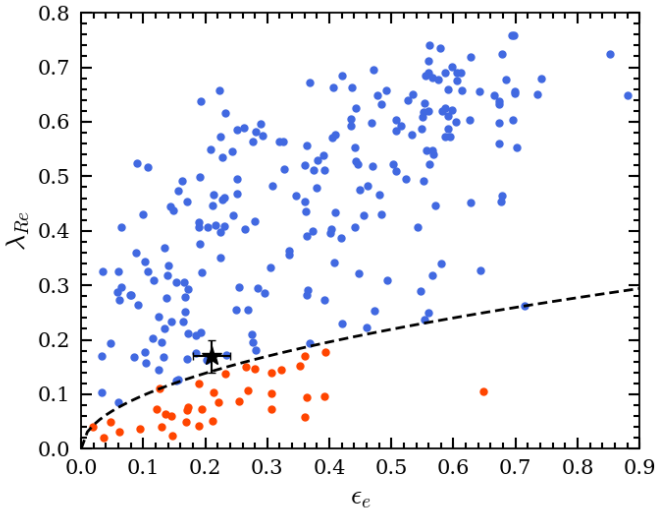


Fig. 5. Specific angular momentum $\lambda_{R_{\rm eff}}$ against ellipticity $\epsilon_{\rm eff}$. The measured value for NGC 7252 $\lambda_{R_{\rm eff}} = 0.17 \pm 0.03$ is shown as the black star and compared to the fast (blue) and slow (red) rotating early-type galaxies as obtained from the ATLAS^{3D} survey (Emsellem et al. 2011). The black dashed line represents the proposed dividing line $\lambda_{R_{\rm eff}} = 0.31\sqrt{\epsilon_{\rm eff}}$ proposed by Emsellem et al. (2011).

Lokas 2017), which needs to be explored to infer the particular conditions for NGC 7252 and is beyond of the scope of this paper.

This merger configuration is likely reflected in the stellar velocity dispersion map which reveals an elongation spanning some 40″ (13 kpc). The primary axis of this high velocity dispersion elongation seems to be orientated nearly along the isophotal semi-major axis within the nearly orthogonal axes of oblate and prolate-like stellar kinematics. Hence, the high velocity dispersion might be primarily caused by the superposition of two different stellar bodies co-existing within intersecting orbital planes. This is qualitatively supported by the structure in the stellar population history as shown later in Fig. 9.

Another notable feature in the stellar kinematics is an isolated bin just west of the nucleus, which seems to be orbiting counter to the adjacent stars. When compared to photometry, this bin is revealed to be the extensively studied super star cluster W3 (e.g. Maraston et al. 2004; Bastian et al. 2013; Cabrera-Ziri et al. 2016). The connection between the star formation history of W3 and that of NGC 7252 will be explored later in section 3.6. A similar bin is also found southeast of the nucleus, corresponding to the super star cluster W30.

3.4. Ionisation conditions

The inner regions of NGC 7252 are rich in ionised gas, particularly in the central star-forming nuclear star forming disc, the [O III] nebulae to the south-west, and a north-easterly gas stream, as shown in Fig. 3. The innermost regions show intense Hβ emission, as shown in panel c of Fig. 3. Most of the Hβ surface brightness is relatively flat, and concentrated within the star-forming disc. It is also asymmetric, with increased brightness to the south and east. There is slight decrease in the Hβ surface brightness within the central 1″, which has been previously found in high-resolution narrow-band imaging (Schweizer et al. 2013). The Hβ distribution falls off quickly towards the edges of the nuclear star forming disc, and remains relatively flat in the annulus immediately outside. Hβ does not, however, feature strongly in the two outer gas streams.

In contrast, the [O III] flux in panel g of Fig. 3 is centrally concentrated. The distribution falls off much more steeply at all radii, never remaining flat. This may suggest a different ionisation mechanism in the central <1″. [O III] does not reach far beyond the nuclear star forming disc, and hence does not feature strongly in the annulus immediately outside. However, the [O III] flux is dominant in the SW gas stream.

To explore the ionisation conditions of NGC 7252, we construct a line ratio diagnostic diagram (Fig 6). Since the wavelength coverage of VIMOS prohibits us from constructing the classical [O III]/Hβ versus [N II]/Hα diagram (Baldwin et al. 1981), we replace [N II]/Hα with the ([N I] $\lambda\lambda$5197,5200)/Hβ line ratio. This surrogate line ratio has been exploited successfully by Sarzi et al. (2010).

While the S/N for all lines is high enough in individual spaxels within the central 12″, examining the properties of the extended gas streams requires co-adding spaxels in order to obtain a reasonable S/N. However, even co-added, the spectra lack detection of the weak [N I] doublet. Hence, we determine 3σ upper limits based on the noise of the co-added spectra. The resulting line ratios for the NE and SW gas streams are indicated in Fig 6, respectively.

To infer the relevant ionisation mechanisms for each region in the galaxy, we compare the measured line ratios with dusty AGN photoionisation models (Groves et al. 2004), shock-ionisation models (Allen et al. 2008), and starburst photoionisation models (Levesque et al. 2010). The outer regions of the nuclear star forming disc feature shock-driven photoionisation. Moving inwards, we see a smooth transition to towards star formation as the dominant ionisation source. However, the trend reverses again at ∼2 arcsec (0.7 kpc) at which the gas excitation is increasing again towards shock and AGN ionisation with decreasing distance from the centre. We suspect this is due to

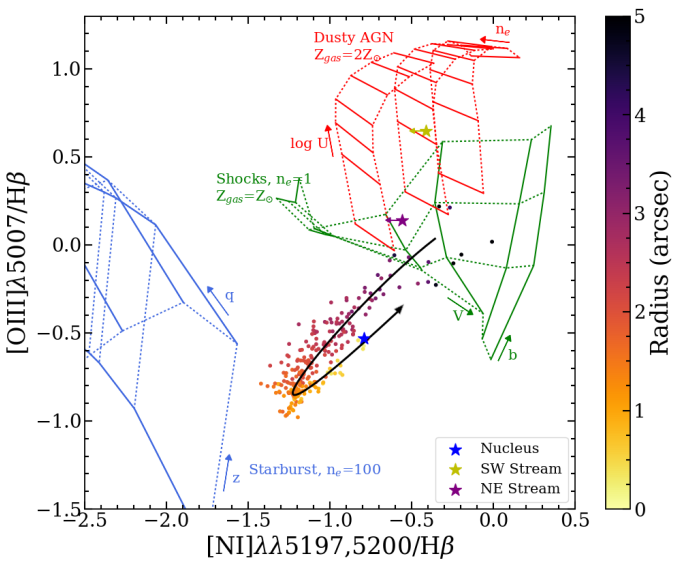


Fig. 6. Diagnostic diagram for the inner 5″ of NGC 7252. Each point corresponds to a pixel, coloured by radius from the centre of the star forming disc. We highlight the systematic trend of the changing-line ratios with decreasing radius by the curved black arrow. Due to low S/N, we are forced to co-add the outer SW and NE gas streams, and determine an upper limit on N I. For comparison we highlight model grids based on AGN photoionisation (red, Groves et al. 2004), shock ionisation (green, Allen et al. 2008), starburst photoionisation (blue, Levesque et al. 2010) for an instantaneous burst with an age of 1 Myr.

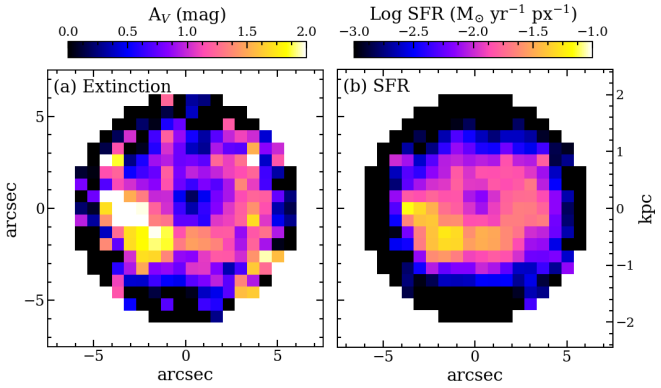


Fig. 7. Extinction and SFR maps of the central starburst derived from gas flux measurements with PyParadise. *Panel a* shows the A_V extinction calculated from the observed Hβ/Hγ line ratios based on the Milky Way extinction law (Cardelli et al. 1989). *Panel b* shows the estimated map of the SFR per pixel based on the extinction-corrected Hβ luminosity and the prescription of Calzetti (2013) after conversion to Hα luminosity. No signature of ongoing star formation have been identified outside of the central 12″ based on emission-line diagnostics.

an additional ionisation mechanisms at play in the centre of NGC 7252, possibly due to a low-luminosity AGN, which is discussed in section 4.3. At very large radii the co-added emission lines ratios of the NE and SW gas streams both reveal signs of either shocked- or AGN-dominated ionisation, consistent with the bright [O III] flux seen in panels g and h of Fig. 3. In particular, the high ionization of the SW stream is consistent with the results of the narrow-band imaging of Schweizer et al. (2013), who argued that this region may be the light echo of a recent AGN episode.

3.5. Conditions for ongoing star formation

The nuclear star forming disc is the only site of active star formation in the 50″ × 50″ FoV, as evidenced by the aforementioned diagnostic plot shown in Fig. 6. Here, we determine the SFR based on the dust-corrected Balmer line fluxes. While usually Hα is employed to count the number of OB stars from their well-known ionising flux, we use the Hβ line converted to the corresponding Hα flux.

We can begin to understand the spatially-resolved dust extinction for NGC 7252 by examining the Hβ/Hγ line ratio map shown in panel d of Fig. 3. Going further, the dust extinction map shown in panel a of Fig. 7 is derived from the measured Hγ/Hβ line ratio for which we assume an intrinsic line ratio of 0.468 by adopting Case B recombination with $T_e = 10^4$ K and $n_e = 10^2$cm^{-3} (Osterbrock & Ferland 2006), and the Milky Way extinction law of Cardelli et al. (1989). The mean extinction within the central 12″ region is found to be 0.65 mag.

In examining both the Balmer ratio and the dust extinction map, one may note the apparent ring structure first seen in studies of the ionised gas by Schweizer (1982) and then of the molecular gas by Wang et al. (1992). We also note a relatively high extinction region in the western portion of the ring, which corresponds to dust features seen in optical imaging, as well as the asymmetric Hβ distribution mentioned in section 3.1.

To use Hα as a SFR calibration, we first compute the dust-corrected Hα flux from Hβ adopting an intrinsic Hα/Hβ line ratio of 2.863 which is based consistently on Case B conditions with $T_e = 10^4$ K and $n_e = 10^2$cm^{-3} (Osterbrock & Ferland 2006). This leads to an integrated dust-corrected Hα luminosity of $L_{\mathrm{H}\alpha} = (3.9 \pm 0.4) \times 10^{41}$erg s^{-1} from which we then calculate the SFR using the prescription of Calzetti (2013) given by

$$\mathrm{SFR}(\mathrm{H}\alpha)/[M_\odot \mathrm{yr}^{-1}] = 5.5 \times 10^{-42} L_{\mathrm{H}\alpha}(\mathrm{erg\ s}^{-1}), \quad (1)$$

which assumes a Kroupa initial mass function (Kroupa 2001) and Case B conditions consistent with our dust correction procedure. The resulting star formation rate map is shown in panel b of Fig. 7 which is clipped to show only pixels predominately ionised by star formation, as indicated by the diagnostic plot in Fig. 6. The corresponding SFR within the VIMOS FoV is computed to be $\mathrm{SFR}(\mathrm{H}\alpha) = 2.2 \pm 0.6\, M_\odot\, \mathrm{yr}^{-1}$. Since star formation is also known to happen far away from the galaxy centre in the tidal tails of NGC 7252 (e.g. Lelli et al. 2015), we also estimated the total SFR. FIR fluxes were measured by *AKARI* (Kawada et al. 2007) which are $f_{90\mu\mathrm{m}} = 5.1$ Jy and $f_{140\mu\mathrm{m}} = 6.4$ Jy as listed in the point source catalogue (Yamamura et al. 2010). Following the prescription of Takeuchi et al. (2010) we compute an FIR-based SFR of $\mathrm{SFR(FIR)} = 6.7\, M_\odot\, \mathrm{yr}^{-1}$ also for a Kroupa IMF. Hence, a substantial fraction of the total star formation is confined to the central few kpc.

CO(1-0) measurements of NGC 7252 obtained by ALMA have provided a molecular gas mass of 4.3×10^9 $M_\odot$ for the inner gas disc (Ueda et al. 2014). Hence, we calculate a molecular depletion time of $t_{\mathrm{dep}} = 1.9 \pm 0.6$ Gyr. This is surprisingly close to the average molecular depletion time of 2.35 Gyr for normal star forming disc galaxies (Bigiel et al. 2011), but shorter than expected from quiescent elliptical galaxies (e.g. Saintonge et al. 2012). While gas-rich early-type galaxies (Davis et al. 2014) exhibit on average a factor of ∼2.5 lower depletion times, the depletion time can be as short as for normal galaxies if the molecular gas is located more the flat part of galaxies rotation curve.

Based on the results above we explore the location of NGC 7252 in the sSFR–M_* plane (Fig. 8). We use the archival

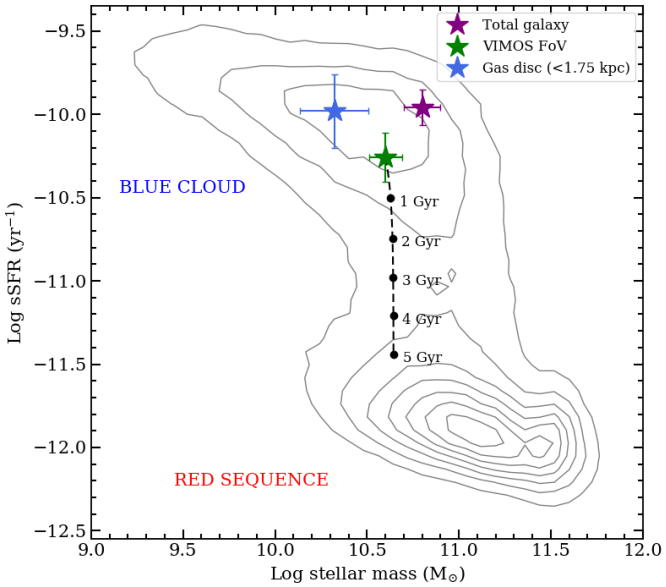


Fig. 8. Specific SFR (sSFR) against stellar mass for NGC 7252 corresponding to the total galaxy (purple), VIMOS field-of-view (green), and nuclear star forming disc (blue). The bimodal galaxy distribution from SDSS MPA-JHU catalog (Kauffmann et al. 2003; Brinchmann et al. 2004) is shown as contours for comparison. Assuming a constant depletion timescale of $t_{\rm dep} = 1.9 \pm 0.6$ Gyr for NGC 7252 based on the molecular gas mass derived from CO(1-0) (Ueda et al. 2014) we predict the position of NGC 7252 for the next 5 Gyr in case of simple gas consumption.

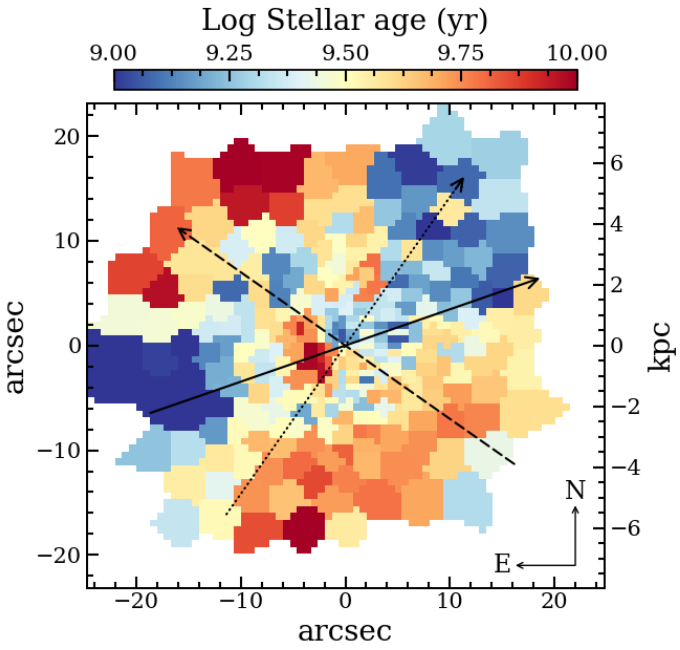


Fig. 9. Luminosity-weighted mean stellar ages from PyParadise. Ages are determined from the stellar population templates used to model the stellar continuum from each Voronoi co-added bin. The younger blue population is spatially distinct from the older population in red. Arrows indicating position angles of the primary stellar rotation axis (solid), primary isophotal axis (dashed), and prolate-like rotation (dotted) are borrowed from Fig. 3.

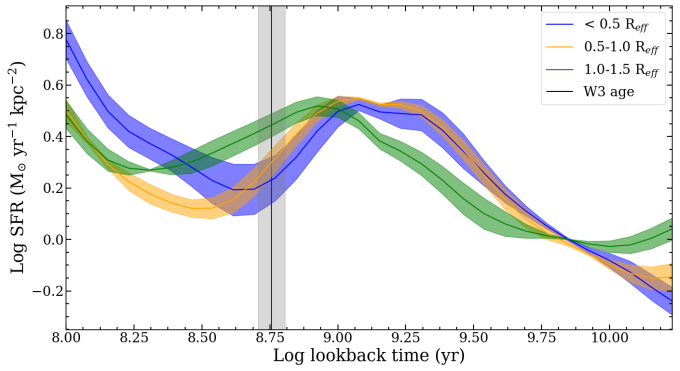


Fig. 10. Star formation histories binned by effective radius. Each curve is binned by 0.5 effective radius, with errors determined from the standard deviation within each spatial bin at a given age. The black vertical line indicates the age of the associated super star cluster W3 as reported by Cabrera-Ziri et al. (2016), with the uncertainty shown in grey.

Hubble WFC3 images of NGC 7252 in the F475W (Sloan g) and F775W (Sloan i) filters to infer a brightness of $m_g = 12.56$ mag (AB) and $m_i = 11.80$ mag (AB), respectively, within an aperture of 30″ radius. Following the empirical stellar mass calibration of Taylor et al. (2011),

$$\log(M_*/[M_\odot]) = 1.15 + 0.7(g - i) - 0.4M_i \quad (2)$$

we compute a stellar mass for NGC 7252 of $\log(M_*/[M_\odot]) = 10.6 \pm 0.1$. Compared to the total stellar mass through a 80″ radius aperture, the VIMOS FoV actually covers 70% of the stellar mass. Together with the SFR computed for the VIMOS FoV and total galaxy as described above, we compute specific star formation rates (sSFRs) of $(5.4 \pm 1.9)\times10^{-11}$ yr^{-1} and $(11 \pm 3)\times10^{-11}$ yr^{-1} for the VIMOS FoV and the total galaxy, respectively. Comparing this to the distribution of local galaxies from the SDSS MPA/JHU galaxy catalogs (e.g. Kauffmann et al. 2003; Brinchmann et al. 2004) we find that, NGC 7252 is still located in the blue cloud of star forming galaxies. We note that the region of ongoing star formation is much smaller than the host galaxy. Hence, we calculate the sSFR using the dynamical mass of the nuclear star forming disc as described in section 3.2, which is marked in Fig. 8. Since the mass of the star forming disc is smaller than the total mass by a factor of three within the VIMOS FoV, the sSFR of this region is right on the main sequence of star formation. This suggests that the galaxy still contains a settled disc component, which has strong implications for the future evolution of NGC 7252 as discussed later in section 4.4.

3.6. Star formation history

We use the STEllar Content and Kinematics from high-resolution galactic spectra via Maximum A Posteriori code (STECKMAP, Ocvirk et al. 2006b,a) to measure star formation histories (SFHs) across the VIMOS FoV. STECKMAP recovers age and metallicity distributions in a non-parametric way, by fitting the full observed spectrum. In practice, STECKMAP minimizes the objective function Q_μ defined as

$$Q_\mu = \chi^2(\mathbf{x}, \mathbf{Z}, \mathbf{g}) + P_\mu(\mathbf{x}, \mathbf{Z}, \mathbf{g}) \quad (3)$$

where $\mathbf{x}$ and $\mathbf{Z}$ are the age and metallicity distributions, and $\mathbf{g}$ is the discretised line of sight velocity distribution (LOSVD). The term P_μ is the penalisation function

$$P_\mu = \mu_{\mathbf{x}} P(\mathbf{x}) + \mu_{\mathbf{Z}} P(\mathbf{Z}) + \mu_{\mathbf{v}} P(\mathbf{g}) \quad (4)$$

This penalisation favours smooth solutions and, effectively, it acts as a Gaussian prior $f_{\rm prior} = e^{-\mu P}$ (Ocvirk et al. 2006b). No-

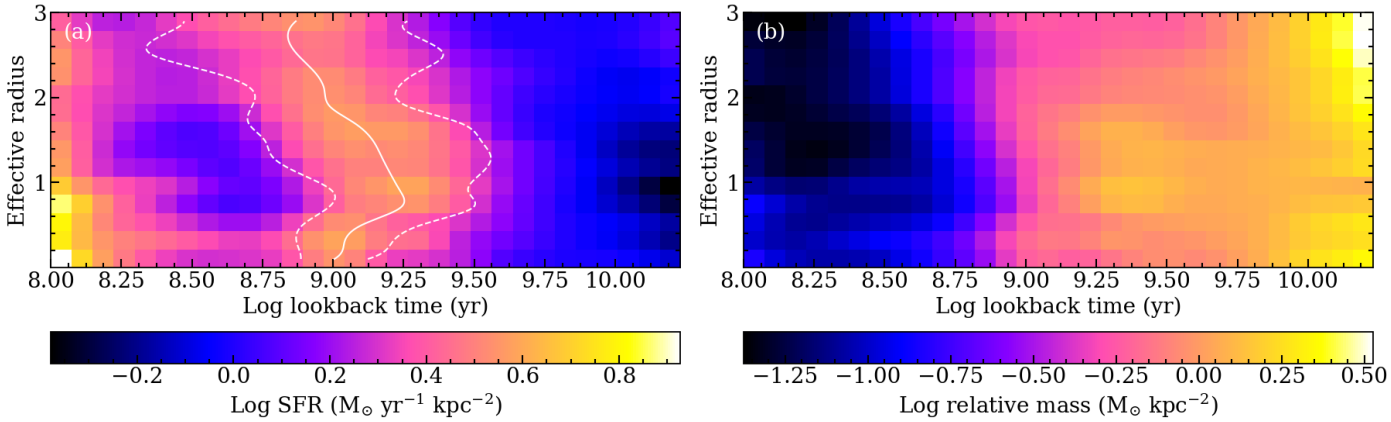


Fig. 11. Summary of the star formation history of NGC 7252 obtained with STECKMAP, normalised over each annulus. *Panel a* shows the SFR as a function of effective radius, measured across cosmic time. The white solid and dotted lines outline the mean and standard deviation of the initial star formation episode. The current star formation episode is clearly visible in the lower left-hand corner. Similarly, *panel b* shows the stellar mass gained at a given time. As expected, most of the mass was built up slowly, beginning at early times with a second peak around 1 Gyr.

tice that the penalisation coefficients μ are set separately for the age, metallicity, and LOSVD distributions.

Although STECKMAP allows for a simultaneous recovery of both stellar populations and kinematical properties, it has been shown that metallicity and stellar velocity dispersion are degenerate parameters (Koleva et al. 2008). However, this degeneracy can be safely broken by first measuring the discretised LOSVD, and then fixing it while measuring the stellar population properties (Sánchez-Blázquez et al. 2011). The LOSVD measurements are already performed with PyParadise as described in section 3.3 and used as inputs for STECKMAP.

We feed STECKMAP with the MILES stellar populations synthesis models (Vazdekis et al. 2010). This set of models ranges from −1.3 to −0.22 dex in metallicity, and from 67 Myr to 17 Gyr in age. We note that the MILES base models follow the solar neighbourhood abundance pattern, meaning that they are [Mg/Fe]-enhanced at low metallicities, but [Mg/Fe] ~ 0 for [Fe/H] $\gtrsim 0$. We keep the stellar initial mass function fixed to that measured in the Milky Way (Kroupa 2001). Since the S/N drops significantly on the blue end of the spectra, we limit our analysis to wavelengths between $\lambda = 4500$Å and $\lambda = 5500$Å. For this work, we assume $\mu_{\mathbf{x}} = \mu_{\mathbf{z}} = 20$. This choice is motivated by a joint comparison between the minimum χ^2 value and the structure of the SFHs. Large μ values lead to smoother solutions, therefore losing time-resolution, but assuming low μ values would produce artefacts on the recovered age and metallicity distributions. The choice of a reliable μ vector is not trivial, but does not affect the overall shape of the SFHs. We have assessed this point by varying the adopted μ values, finding no significant differences in our results.

Finally, the age distributions recovered using STECKMAP are translated to mass fractions and SFRs as a function of lookback time, as demonstrated in Fig. 10 and Fig. 11. The recovered SFHs strengthen the story of NGC 7252 as a merger remnant. Fig. 10 demonstrates that the SFR peaked roughly 1 Gyr ago whereby the burst occurred slightly earlier in the innermost region (blue) than in the outer regions (orange, then green) at a similar SFR. The current episode of rapid star formation is significantly stronger in the inner region.

Not only does the merger age estimate of 0.6 Gyr as suggested by Schweizer (1982) fit well into this picture, but also the estimated age of 570 Myr for star cluster W3 as inferred by Cabrera-Ziri et al. (2016). In contrast, the star formation history of the entire galaxy appears significantly extended over several 100 Myr during the merger period, more than just a single burst. We will discuss the relation of this extended star formation with its spatial distribution as a result of the merger in the following section.

4. Discussion

4.1. Prolate-like rotation from a gas-rich major merger

Early-type galaxies are usually rotation around their minor axis (oblate rotation), if they regularly rotate at all. Evidence for systems with rotation around the major axis (prolate-like rotation) instead is currently scarce. After many unsuccessful searches (e.g. Bertola et al. 1988), there are currently about a dozen early-type galaxies known to have clear signatures of prolate-like rotation (e.g. Schechter & Gunn 1979; Wagner et al. 1988; Krajnović et al. 2011; Emsellem et al. 2014). IFU surveys like CALIFA (Sánchez et al. 2012), MaNGA (Bundy et al. 2015) or the Most Massive MUSE Galaxies (M3G) survey (PIs: Emsellem & Krajnović) are working to increase the number of galaxies with signatures of prolate-like rotation.

The nature and origin of the prolate-like rotation in early-type galaxies is still under debate. Satellite accretion, as well as major mergers of nearly equal mass have become the two leading formation scenarios (Ebrova & Lokas 2017; Li et al. 2018). Tsatsi et al. (2017) has discovered ten early-type galaxies in CALIFA with signatures of prolate-like rotation, which corresponds to 9% of all early-type galaxies in the same volume. By comparing the observations with N-body simulations they showed that the prolate-like rotation can be produced by a major polar merger. As NGC 7252 has formed from the merger of two disc galaxies, it is very likely that its formation mechanism and observed prolate-like rotation are indeed related. We therefore expect that some part of the angular momentum vectors, composed of the orbital and rotational vectors, should be perpendicular to each other. Whether the prolate-like rotation is predominately produced by one of those angular momentum components is unclear at this point. However, the vast majority of presently known galaxies with prolate-like rotation are found in dense environments and have little or no gas. NGC 7252 is in both ways different from those, suggesting its formation mechanism is different than other known cases. Alternatively, with NGC 7252 we

are witnessing the early, still gas rich, stage of the formation of a future classical elliptical with complex kinematics.

Binary mergers are known to produce galaxies with prolate-like rotation (e.g. Naab & Burkert 2003), where the actual kinematics, such as the existence of a kinematically decoupled core (KDC), or the change from an oblate-like (centre) to a prolate-like rotation (outskirts) is dependent on the mergers orbit, spins of the progenitors and the gas content (Hoffman et al. 2010; Bois et al. 2011). NGC 7252 still has a considerable amount of gas, $4.5 \times 10^9 M_\odot$ of H I (Hibbard et al. 1994) and $3.5 \times 10^9 M_\odot$ of H_2 (Wang et al. 1992), and its kinematic structure could be viewed as an inner KDC exhibiting an oblate-like (regular) rotation, which changes beyond 10″ (3.3 kpc) into a prolate-like rotation. The velocity map of NGC 7252 resembles those of binary merger simulations of Hoffman et al. (2010) with gas fractions of 20% or more. In these simulations, the gas is responsible for building the short-axis tubes and the regular rotation in the centre, while the outer prolate-like rotation (built of long-axis tubes) can appear in various combinations of the orbital parameters and progenitor spins, and does not necessarily require a polar orbit. Similar conclusions are also found in Bois et al. (2011).

The first numerical simulations of NGC 7252 by Borne & Richstone (1991) and Mihos et al. (1993) employed a retrograde merger of disc galaxies to account for the presumably counter-rotating gas disc reported by Schweizer (1982). Later, Hibbard & Mihos (1995) presented a new self-consistent N-body simulation based solely on the large-scale H I kinematics obtained with the Very Large Array. In this model, the inclination of two progenitor galaxies are $i_1 = -40°$ and $i_2 = 70°$ with respect to the merger plane, which would imply perpendicular orbital angular momentum vectors, consistent with a polar merger geometry. However, various other configurations may also be able to produce the observed stellar kinematics that need to be systematically tested by varying the initial conditions of this merger in terms of mass ratio, impact parameter, orbital and spin angular momentum. As stars are collisionless particles, in contrast to the gas, they can probe the kinematics down to the centre of the remnant galaxy, void of H I gas. While performing matched N-body simulations is beyond the scope of this paper, our stellar kinematic field should provide valuable constraints on merger parameters for future hydrodynamical simulations.

4.2. The star formation history during the merger event

NGC 7252 provides a snapshot in the evolution of two spiral galaxies into an elliptical. Dedicated numerical simulations of this particular merger remnant have constrained the time since the pericentre of the two discs to be about 770 Myr in the simulations by Borne & Richstone (1991) and 620 Myr in the simulations by Chien & Barnes (2010). This timescale is supported by the ages of associated massive star clusters lying in the range of 400-600 Myr (Schweizer & Seitzer 1998). The age of the well-studied cluster W3, for example, has been found at 570 Myr (Cabrera-Ziri et al. 2016). The centre of NGC 7252 exhibits a post-starburst spectrum with strong Balmer lines (Fritze-v. Alvensleben & Gerhard 1994), implying a strong starburst event less than 1 Gyr ago and an extended period of star formation starting even before pericentre passage. With our IFU data we are able to explore the star formation history of NGC 7252 for the first time, elucidating the nature of the intense star formation episode coincident with the merger.

One main result of our IFU observation is that the starburst episode is significantly extended over several hundred Myr and suggests star formation activity before, during, and after the time of first pericentre passage. In particular, we show that the peak in star formation activity first occurred near the galaxy centre ($< 1R_{\rm eff}$), moving radially outwards at later times. The extended star formation activity prior to the anticipated time of pericentre passage could be explained by a starburst which had been already triggered in the galaxy core, as the galaxies were approaching the closest point of their first pass. Such enhanced star formation activity at the centre of galaxies has already been measured over large samples of galaxies at separations of $\lesssim$20 kpc (Li et al. 2008; Ellison et al. 2008; Wong et al. 2011; Scudder et al. 2012; Patton et al. 2013; Davies et al. 2015). Hence, it is observationally expected that star formation is already enhanced before the final pericentre passage. This is consistent with numerical simulations of nearly equal mass mergers of disc galaxies, exhibiting the highest SFR excess a few hundred Myr before the final pericentre passage (e.g. Moreno et al. 2015) and a suppression after final coalescence.

Our spatially-resolved SFH also recovers the period of low star formation activity after pericentre, which reaches a minimum around ∼300 Myr ago. The decline in SFR is less effective for the regions which end up at larger radii possibly due to a higher angular momentum than the remnant centre. Those regions may therefore originate primarily from the outskirts of the progenitors rather than the cores and may subject to continuous or enhanced star formation at later time during the merger. The relatively young ages and galacto-centric radius of the star clusters such as W3 matches well with the extended episode of star formation in the outskirts of the merging system. Such a shift in SFR peak from the core to the large scale regions is also reproduced in the numerical simulations by Moreno et al. (2015).

Although the nucleus of NGC 7252 exhibits post-starburst features, ongoing star formation in the central 2 kpc is clearly present. This is readily seen in the current epoch by an increased SFR at small radii, with a similar SFR level appearing to have existed previously ∼ 1 Gyr ago. This on-going star formation activity suggest that the final coalescence of the major merger occurred relatively recently, certainly within the last 200 Myr: numerical simulations of major mergers with masses and dynamical times show that merger-induced star formation stops within 100–200 Myr after the coalescence, even without AGN quenching (Springel et al. 2005a; Bournaud et al. 2011; Torrey et al. 2012; Powell et al. 2013; Moreno et al. 2015). High-resolution hydrodynamic simulations resolving dense gas clouds within merging galaxies have shown that triggered star formation can last longer than previously thought, but only before the coalescence, and rapidly decreases in 100–200 Myr afterwards (e.g. Teyssier et al. 2010; Renaud et al. 2014). Observations also suggest that merger-induced star formation events are short-lived (Ellison et al. 2013).

This also holds for systems at high redshift and/or with high gas fractions (Fensch et al. 2017). Dedicated simulations fitting NGC 7252 by Chien & Barnes (2010) also predict rapidly falling SFR after the starburst phases. In detail these simulations do not predict any recent star formation activity, but their resolution limited to 170 pc for the gravitational softening with a potentially larger SPH smoothing length may miss local events in the nucleus itself – alternatively the true orbit, structure, and kinematics of the progenitor models which merged to form NGC 7252 may somewhat differ from those used in this specific simulation.

Another line of evidence for recent coalescence comes from the bright tidal features visible around NGC7252: such features rarely last more than ∼ 500 Myr (e.g. Duc & Renaud 2013). The study of tidal debris in post-merger systems by Ji et al. (2014) indicates that such debris are likely visible at magnitudes brighter

than 25 mag arcsec^{-2} during 600 Myr or less for systems with the mass of NGC 7252: debris in NGC 7252 is both much brighter than this limit and fairly continuous over tens of kpc, suggesting that the previous value is a strong upper limit to the age of this post-merger system.

These lines of evidence show that the presumably re-formed disc at the centre of NGC 7252 is young, most likely 100-200 Myr-old. Such rapid re-formation of a relaxed and symmetric cold gas disc is consistent with high-resolution simulations of major mergers (e.g. Bournaud et al. 2011; Renaud et al. 2014). The settled gas must have been located in-situ in or near the galaxy nuclei or at least in the inner progenitor galaxy discs, as accretion from the outskirts would require much longer timescales.

Although the SFH of NGC 7252 agree well with generic predictions of merger simulations, some aspects remain puzzling. We anticipate that the spatially-resolved SFH of NGC 7252 will provide useful constraints on the initial conditions of gas content and distribution for tailored simulations of this particular major merger system.

4.3. Low-luminosity AGN or LINER?

One of the most recent discoveries from the study of NGC 7252 is the detection of a bright [O III] nebulosity ∼5 kpc south-west of the galaxy centre by Schweizer et al. (2013). No indication of ongoing black hole (BH) activity at the nucleus has been yet confirmed in the radio and X-rays, and so Schweizer et al. (2013) concluded that NGC 7252 may have hosted an AGN at its centre that has drastically decreased in luminosity in the recent past. NGC 7252 would therefore fall in the same category as Hanny's Voorwerp (Lintott et al. 2009) and other galaxies that display potential AGN light echos (Keel et al. 2015). Our IFU observations also cover this [O III] nebulosity and we confirm the high excitation of the gas. Based on our emission-line diagnostic diagrams as discussed in section 3.4, we also find evidence of an AGN as the dominant ionisation mechanism in this particular region.

In addition, our VIMOS IFU data provides additional constraints on the gas excitation around the nucleus. As shown in Fig. 7, the dust attenuation map and SFR distribution reveal a drop in dust content and Hα luminosity at the galaxy centre. This agrees with a previously reported deficit within the central 1-2″ of Hα from narrow-band images (Schweizer 1982) and molecular gas (Wang et al. 1992). However, the centrally concentrated [O III] emission leads to an enhanced [O III]/Hβ line ratio. The emission-line diagnostic plot (Fig. 6) confirms that the line ratios indeed increase towards higher excitation at the galaxy centre. Schweizer et al. (2013) also compared the line ratios from narrow-slit spectra of the galaxy centre, but only considered a nuclear and a star forming disc size aperture, missing the gradient apparent in the emission profiles. Given the low spatial resolution of our data we cannot avoid a strong contamination of the nuclear emission lines by the bright star-forming disc, in particular for Hβ. The intrinsic line ratios of the nucleus are then likely located in either the shock or the low-luminosity AGN region of the diagram. Only IFU observations at higher spatial resolution may be able to spatially separate the line ratios from the nucleus and the star forming disc.

If we nevertheless interpret the extinction-corrected ($A_V \sim 1.35$ mag) [O III] line flux of $(3.17\pm0.3)\times10^{-15}$ erg/s/cm^2 within the central $4'' \times 4''$ to be excited by a low-luminosity AGN, we would estimate an AGN bolometric luminosity of $L_{\rm bol} = (2.4 \pm 0.3) \times 10^{41}$ erg s^{-1} following the empirical correlation between [O III] and bolometric luminosity from Stern & Laor (2012). The corresponding 2-10 keV luminosity would be 5.9×10^{40} erg s^{-1}, adopting a bolometric correction of $L_{[\rm O\,III]}/L_{2-10\rm keV} \sim 0.03$ from Heckman et al. (2005). This is perfectly consistent with the X-ray luminosity of the nucleus $\log(L_X/[\rm erg\ s^{-1}]) = 40.75^{+0.03}_{-0.04}$ as reported by Nolan et al. (2004) from *Chandra* observations. Hence, the nuclear [O III] and X-ray emission indeed follows the relation implied for BH activity. Schweizer et al. (2013) concluded that most of the X-ray luminosity may originate from star formation from the circumnuclear disc. However, they assume a SFR of 6 $M_\odot$yr^{-1} for the star-forming disc, which is a factor of three higher than we infer from the IFU data as discussed in section 3.5.

In any case, the putative AGN luminosity is still much lower than the luminosity required to excite the [O III] nebulosity as discussed by Schweizer et al. (2013) and their scenario of a recently faded AGN remains valid. These kind of changing-look AGN are observed with increasing numbers (e.g. Denney et al. 2014; LaMassa et al. 2015; Merloni et al. 2015; McElroy et al. 2016). In particular, Mrk 1018 is not only a galaxy in an advanced major merger stage, but also shows AGN flickering on a timescale of a few years. This flickering may possibly be related to the interaction of a binary BH system, accretion disc wind regulation, or other currently unknown scenarios (Husemann et al. 2016). Whether the variability in BH accretion on $10^3 - 10^5$yrs timescales is particularly enhanced during particular phases of a major merger or simply reflects the usual variability of AGN (e.g. Schawinski et al. 2015) remains to be tested.

Alternatively, the emission-line ratios may also point to a Low-Ionisation Nuclear Emission Region (LINER) for which AGN are not necessarily the primary ionisation mechanism. Also, shocks from supernova or the gravitational infall of gas would lead to line ratios consistent with slow shocks. Furthermore, post-AGB stars have become a more favourable interpretation of LINERs in early-type galaxies (e.g. Singh et al. 2013). The high central concentration of [O III] emission also agrees with such a scenario given the steep surface brightness profile of the stellar continuum corresponding to a de Vaucouleurs law (e.g. Schweizer 1982). Again, given our poor spatial resolution, we cannot readily distinguish between a pure point-like or slightly extended [O III] flux distribution. Also, the contamination of Hβ due to the star forming ring is too high to test whether the expected amount of ionising photons from post-AGB stars is sufficient to explain the excitation, as we are using the equivalent width of Hβ (as a surrogate for Hα; Cid Fernandes et al. 2010). In this case, the estimated AGN bolometric luminosity from the [O III] line would be a very strong upper limit, strengthening the fading AGN scenario.

4.4. When will NGC 7252 reach the red sequence?

While NGC 7252 is still located within the blue cloud of star-forming galaxies in colour-magnitude and sSFR-M_* plane, the high Sérsic index of the merger remnant is consistent with the standard evolutionary picture in which the major merger of two star-forming disc galaxies is responsible for the morphological transformation to an elliptical galaxy. Also, a high SFR is predicted to occur at several times during the merger, as discussed above. However, the process of transitioning from a blue cloud to a red sequence galaxy is less clear. On which timescales the stellar populations evolve is a key question, being either a fast or a slow process. The relatively low number density of green valley galaxies implies that the transition phase should be short, lasting much less than 1 Gyr (e.g. Schawinski et al. 2007, 2014). On the contrary, Martin et al. (2007) found a much longer timescale

of 1-6 Gyr for the transition from the blue cloud to the red sequence. Only the latter scenario appears consistent with the gas consumption timescale, which may be the main regulator for the future evolution of NGC 7252. This implies that the transition phase for NGC 7252 is either significantly prolonged and unexpected for gas-rich major mergers, or that other processes such as AGN feedback have yet to kick-in. The later must occur in order to support a rapid quenching of star formation (e.g. Springel et al. 2005a; Di Matteo et al. 2005).

The long transformation time we infer is based on the assumption that the $t_{\rm dep}$ remains unchanged until all the molecular gas is consumed. This timescale may be significantly shortened in the event of another burst in star formation, an increasing fraction of the molecular gas being locked up in the diffuse atomic gas phase and not able to form stars, dynamical suppression of star formation or an expulsion of gas by an AGN. The first option is less likely given that the merger has already passed the coalescence phase and no additional triggering of an enhanced star formation phase is expected in numerical simulations (e.g. Chien & Barnes 2010). In line with the second option, H I-rich elliptical galaxies have been detected and represent roughly 40% of the local ellipticals (Serra et al. 2012) outside of clusters, so it is possible that the final remnant of NGC 7252 will be a H I-rich elliptical galaxy. The dynamical suppression of star formation in early-type galaxies was put forward by Davis et al. (2014), who found that the depletion time was significantly longer for molecular gas located in the rising part of the rotation curve. This mechanisms seem not to apply in the case of NGC 7252 because most of the molecular gas in the star-forming disc is located flat part of the rotation curve as traced by Hα emission (see Fig. 4). Hence, additional tidal forces would be required to bring the gas closer in towards the nucleus on short timescale, which is unlikely to be happen given the advanced evolutionary stage of the merger.

AGN triggering during a major merger is often invoked to rapidly quench star formation by expelling much of the gas with powerful outflows (e.g. Di Matteo et al. 2005). The strong [O III] nebulosity of NGC 7252 already shows that an AGN was likely present in the recent past, as convincingly argued in Schweizer et al. (2013). This is also consistent with the presumed time delay of a few 100 Myr between the peak of star formation and AGN accretion (e.g. Wild et al. 2010; Schawinski et al. 2010). However, no kinematic signature of an AGN-driven outflow on galaxy-scales has yet been detected for NGC 7252. Apparently, the previous AGN phase was either too brief or too weak to develop a galactic outflow. It is unknown when the next AGN phase will be triggered and if it will be powerful enough to develop a sufficiently strong outflow to rapidly quench star formation. The IFU data we present is consistent with the presence of a low-luminosity AGN and an increasing number of AGN are known to change their luminosity on rather short timescales (e.g. Lintott et al. 2009; Denney et al. 2014; LaMassa et al. 2015; McElroy et al. 2016). Even if an AGN will turn on again, it may not be able to affect the settled gas disc, as some simulations have shown that the AGN energy may be able to escape without removing much gas in this configuration (e.g. Gabor & Bournaud 2014). Hence, NGC 7252 already passed the presumed AGN blow-out phase for a purely merger-driven AGN quenching scenario. If the modest gas reservoir currently available to form stars is not first removed by an AGN phase or rapidly depleted by a burst of star formation triggered by dynamical effects (e.g. minor mergers), we conclude that NGC 7252 will eventually die out and become a red elliptical galaxy in several Gyr as predicted for slow transformation scenario (e.g. Martin et al. 2007).

5. Summary and conclusions

Using VLT-VIMOS IFU observations covering the central $50'' \times 50''$ of the recent merger remnant NGC 7252, we obtain maps detailing the stellar and gaseous properties of the galaxy, including kinematics and line strengths. Our major results based on a detailed analysis of these spatially-resolved properties can be summarised by the following:

- We confirm the presence of a central rotating gas disc with a kinematic inclination and maximum velocity in agreement with Ueda et al. (2014) and no signature of counter-rotation as initially reported.
- We find clear signatures of both oblate- and prolate-like rotation which may be caused by a polar merger configuration or a radial orbit with different spin angular momentum vectors.
- A study of the SFH of NGC 7252 indicates an extended period of elevated SFR extending until 1 Gyr ago, reaching beyond the anticipated time of first passage, which highlights a complex radially-dependent SFH produced throughout the galaxy merger.
- We compute a SFR of $2.2 \pm 0.6 M_{\odot} \mathrm{yr}^{-1}$ as measured by the dust-corrected Hα luminosity within the central 7 kpc, corresponding to a molecular gas depletion time of $\sim$2 Gyr given the measured molecular gas mass in this region.
- Higher ionisation conditions of the gas are found at the very centre of NGC 7252 from which we draw an upper limit on $L_{\rm bol} < 2.4 \times 10^{41}$ erg s^{-1} based on the [O III] luminosity, consistent with the X-ray luminosity of the nucleus.
- NGC 7252 is still within the blue cloud of galaxies as seen in the sSFR–M_* plane and assuming a constant molecular gas depletion time we infer a transitional time of about 5 Gyr until it reaches the red sequence through gas consumption.

Given that NGC 7252 is one of the nearest major merger remnants of two disc galaxies, it has been employed as a Rosetta stone in understanding the transformational process from star-forming disc galaxies to quiescent elliptical galaxies. Our IFU observations provide a suite of new diagnostics such as prolate-like rotation in the stellar components and a complex spatially-resolved star formation history. All of this information needs to be interpreted alongside dedicated numerical simulations of major mergers, which can now be better tuned to NGC 7252, beyond the scope of this work.

The past history of NGC 7252 seems more and more settled as simulations and observations are converging to a common picture. The final destiny however, still remains open. While NGC 7252 has already transformed into an early-type galaxy based on the light profile, it remains as a blue cloud galaxy based on colours and SFR. A detailed analysis of the star formation history and tidal debris suggests that the central gas disc has presumably re-formed quickly in within 100 Myr since central coalescence of the major merger, most likely from in-situ material rather than infall from the galaxy outskirts. Hence, the transformation from two blue disc galaxies to a quiescent elliptical is far from complete as a significant portion of the transformation has not yet begun. It seems the destiny of NGC 7252 cannot be constrained nor predicted at this point. The most plausible scenario is that the galaxy will likely evolve on the timescale of several Gyr as it slowly consumes the remaining gas. However, we cannot predict further events, such as an intense AGN period, that could rapidly accelerate this process.

Although NGC 7252 provides a strong proof of concept that two disc galaxies can be transformed into an elliptical on rather short timescales, it cannot be used to study the complete transformational process to quiescence. Detailed observations of similar

major merger remnants within a range of several 100 Myr before and a few Gyr after first pericentre passage are still required to constrain physical prescriptions of merger simulations and fully understand the evolution in star formation in galaxy mergers.

Acknowledgements. We thank the anonymous referee for their comments which improved our original manuscript. We also extend a special thanks to Glenn van de Ven for helpful discussion about the project. JW acknowledges financial support and thanks Max Planck Institute for Astronomy for the great hospitality during his two month summer student internship in 2017, during which the majority of this work was performed. IMN acknowledges funding from the Marie Skłodowska-Curie Individual Fellowship 702607, and from grant AYA2013-48226-C3-1-P from the Spanish Ministry of Economy and Competitiveness (MINECO). RMcD is the recipient of an Australian Research Council Future Fellowship (project number FT150100333).

References

Allen, M. G., Groves, B. A., Dopita, M. A., Sutherland, R. S., & Kewley, L. J. 2008, ApJS, 178, 20
Baldwin, J. A., Phillips, M. M., & Terlevich, R. 1981, PASP, 93, 5
Barnes, J. E. 1992, ApJ, 393, 484
Barnes, J. E. 2004, MNRAS, 350, 798
Bastian, N., Schweizer, F., Goudfrooij, P., Larsen, S. S., & Kissler-Patig, M. 2013, MNRAS, 431, 1252
Bertola, F., Galletta, G., Capaccioli, M., & Rampazzo, R. 1988, A&A, 192, 24
Bigiel, F., Leroy, A. K., Walter, F., et al. 2011, ApJ, 730, L13
Bois, M., Emsellem, E., Bournaud, F., et al. 2011, MNRAS, 416, 1654
Borne, K. D. & Richstone, D. O. 1991, ApJ, 369, 111
Bournaud, F., Chapon, D., Teyssier, R., et al. 2011, ApJ, 730, 4
Bournaud, F., Jog, C. J., & Combes, F. 2005, A&A, 437, 69
Bradley, L., Sipocz, B., Robitaille, T., et al. 2017, astropy/photutils: v0.4
Brinchmann, J., Charlot, S., White, S. D. M., et al. 2004, MNRAS, 351, 1151
Bundy, K., Bershady, M. A., Law, D. R., et al. 2015, ApJ, 798, 7
Cabrera-Ziri, I., Bastian, N., Hilker, M., et al. 2016, MNRAS, 457, 809
Calzetti, D. 2013, Star Formation Rate Indicators, ed. J. Falcón-Barroso & J. H. Knapen, 419
Cappellari, M. & Copin, Y. 2003, MNRAS, 342, 345
Cappellari, M., Emsellem, E., Bacon, R., et al. 2007, MNRAS, 379, 418
Cappellari, M., Emsellem, E., Krajnović, D., et al. 2011, MNRAS, 413, 813
Cardelli, J. A., Clayton, G. C., & Mathis, J. S. 1989, ApJ, 345, 245
Chien, L.-H. & Barnes, J. E. 2010, MNRAS, 407, 43
Cid Fernandes, R., Stasińska, G., Schlickmann, M. S., et al. 2010, MNRAS, 403, 1036
Croom, S. M., Lawrence, J. S., Bland-Hawthorn, J., et al. 2012, MNRAS, 421, 872
Davies, L. J. M., Robotham, A. S. G., Driver, S. P., et al. 2015, MNRAS, 452, 616
Davis, T. A., Alatalo, K., Sarzi, M., et al. 2011, MNRAS, 417, 882
Davis, T. A., Young, L. M., Crocker, A. F., et al. 2014, MNRAS, 444, 3427
de Zeeuw, P. T., Bureau, M., Emsellem, E., et al. 2002, MNRAS, 329, 513
Denney, K. D., De Rosa, G., Croxall, K., et al. 2014, ApJ, 796, 134
Di Matteo, P., Bournaud, F., Martig, M., et al. 2008, A&A, 492, 31
Di Matteo, T., Springel, V., & Hernquist, L. 2005, Nature, 433, 604
Duc, P.-A. & Renaud, F. 2013, in Lecture Notes in Physics, Berlin Springer Verlag, Vol. 861, Lecture Notes in Physics, Berlin Springer Verlag, ed. J. Souchay, S. Mathis, & T. Tokieda, 327
Ebrova, I. & Lokas, E. L. 2017, ArXiv e-prints [arXiv:1708.03311]
Ellison, S. L., Mendel, J. T., Patton, D. R., & Scudder, J. M. 2013, MNRAS, 435, 3627
Ellison, S. L., Patton, D. R., Simard, L., & McConnachie, A. W. 2008, AJ, 135, 1877
Emsellem, E., Cappellari, M., Krajnović, D., et al. 2011, MNRAS, 414, 888
Emsellem, E., Cappellari, M., Krajnović, D., et al. 2007, MNRAS, 379, 401
Emsellem, E., Cappellari, M., Peletier, R. F., et al. 2004, MNRAS, 352, 721
Emsellem, E., Krajnović, D., & Sarzi, M. 2014, MNRAS, 445, L79
Falcón-Barroso, J., Lyubenova, M., van de Ven, G., et al. 2017, A&A, 597, A48
Falcón-Barroso, J., Sánchez-Blázquez, P., Vazdekis, A., et al. 2011, A&A, 532, A95
Fensch, J., Renaud, F., Bournaud, F., et al. 2017, MNRAS, 465, 1934
Fritze-v. Alvensleben, U. & Gerhard, O. E. 1994, A&A, 285, 775
Fruchter, A. S. & Hook, R. N. 2002, PASP, 114, 144
Gabor, J. M. & Bournaud, F. 2014, MNRAS, 441, 1615
Genel, S., Vogelsberger, M., Springel, V., et al. 2014, MNRAS, 445, 175
Groves, B. A., Dopita, M. A., & Sutherland, R. S. 2004, ApJS, 153, 9
Heckman, T. M., Ptak, A., Hornschemeier, A., & Kauffmann, G. 2005, ApJ, 634, 161
Hernquist, L. & Barnes, J. E. 1991, Nature, 354, 210
Hibbard, J. E., Guhathakurta, P., van Gorkom, J. H., & Schweizer, F. 1994, AJ, 107, 67
Hibbard, J. E. & Mihos, J. C. 1995, AJ, 110, 140
Ho, I.-T., Kewley, L. J., Dopita, M. A., et al. 2014, MNRAS, 444, 3894
Hoffman, L., Cox, T. J., Dutta, S., & Hernquist, L. 2010, ApJ, 723, 818
Hopkins, P. F., Cox, T. J., Hernquist, L., et al. 2013, MNRAS, 430, 1901
Hopkins, P. F., Hernquist, L., Cox, T. J., & Kereš, D. 2008, ApJS, 175, 356
Horne, K. 1986, PASP, 98, 609
Husemann, B., Jahnke, K., Sánchez, S. F., et al. 2013, A&A, 549, A87
Husemann, B., Jahnke, K., Sánchez, S. F., et al. 2014, MNRAS, 443, 755
Husemann, B., Urrutia, T., Tremblay, G. R., et al. 2016, A&A, 593, L9
Ji, I., Peirani, S., & Yi, S. K. 2014, A&A, 566, A97
Kauffmann, G., Heckman, T. M., White, S. D. M., et al. 2003, MNRAS, 341, 33
Kawada, M., Baba, H., Barthel, P. D., et al. 2007, PASJ, 59, S389
Keel, W. C., Maksym, W. P., Bennert, V. N., et al. 2015, AJ, 149, 155
Koleva, M., Prugniel, P., Ocvirk, P., Le Borgne, D., & Soubiran, C. 2008, MNRAS, 385, 1998
Krajnović, D., Alatalo, K., Blitz, L., et al. 2013, MNRAS, 432, 1768
Krajnović, D., Bacon, R., Cappellari, M., et al. 2008, MNRAS, 390, 93
Krajnović, D., Emsellem, E., Cappellari, M., et al. 2011, MNRAS, 414, 2923
Kroupa, P. 2001, MNRAS, 322, 231
Kuntschner, H., Emsellem, E., Bacon, R., et al. 2010, MNRAS, 408, 97
LaMassa, S. M., Cales, S., Moran, E. C., et al. 2015, ApJ, 800, 144
Le Févre, O., Saisse, M., Mancini, D., et al. 2003, in in Proc. SPIE, ed. M. Iye & A. F. M. Moorwood, Vol. 4841, 1671–1681
Lelli, F., Duc, P.-A., Brinks, E., et al. 2015, A&A, 584, A113
Levesque, E. M., Kewley, L. J., & Larson, K. L. 2010, AJ, 139, 712
Li, C., Kauffmann, G., Heckman, T. M., White, S. D. M., & Jing, Y. P. 2008, MNRAS, 385, 1915
Li, H., Mao, S., Emsellem, E., et al. 2018, MNRAS, 473, 1489
Lintott, C. J., Schawinski, K., Keel, W., et al. 2009, MNRAS, 399, 129
Lotz, J. M., Jonsson, P., Cox, T. J., et al. 2011, ApJ, 742, 103
Ma, C.-P., Greene, J. E., McConnell, N., et al. 2014, ApJ, 795, 158
Maraston, C., Bastian, N., Saglia, R. P., et al. 2004, A&A, 416, 467
Martin, D. C., Wyder, T. K., Schiminovich, D., et al. 2007, ApJS, 173, 342
McElroy, R., Husemann, B., Croom, S. M., et al. 2016, A&A, 593, L8
Merloni, A., Dwelly, T., Salvato, M., et al. 2015, MNRAS, 452, 69
Mihos, J. C., Bothun, G. D., & Richstone, D. O. 1993, ApJ, 418, 82
Monreal-Ibero, A., Arribas, S., Colina, L., et al. 2010, A&A, 517, A28
Moreno, J., Torrey, P., Ellison, S. L., et al. 2015, MNRAS, 448, 1107
Naab, T. & Burkert, A. 2003, ApJ, 597, 893
Naab, T., Oser, L., Emsellem, E., et al. 2014, MNRAS, 444, 3357
Nolan, L. A., Ponman, T. J., Read, A. M., & Schweizer, F. 2004, MNRAS, 353, 221
Ocvirk, P., Pichon, C., Lançon, A., & Thiébaut, E. 2006a, MNRAS, 365, 74
Ocvirk, P., Pichon, C., Lançon, A., & Thiébaut, E. 2006b, MNRAS, 365, 46
Osterbrock, D. E. & Ferland, G. J. 2006, Astrophysics of gaseous nebulae and active galactic nuclei (2nd. ed. by D.E. Osterbrock and G.J. Ferland. Sausalito, CA: University Science Books, 2006)
Patton, D. R., Torrey, P., Ellison, S. L., Mendel, J. T., & Scudder, J. M. 2013, MNRAS, 433, L59
Powell, L. C., Bournaud, F., Chapon, D., & Teyssier, R. 2013, MNRAS, 434, 1028
Renaud, F., Bournaud, F., Kraljic, K., & Duc, P.-A. 2014, MNRAS, 442, L33
Richtler, T., Husemann, B., Hilker, M., et al. 2017, A&A, 601, A28
Rodriguez-Gomez, V., Genel, S., Vogelsberger, M., et al. 2015, MNRAS, 449, 49
Rothberg, B. & Joseph, R. D. 2004, AJ, 128, 2098
Saintonge, A., Tacconi, L. J., Fabello, S., et al. 2012, ApJ, 758, 73
Sánchez, S. F., Kennicutt, R. C., Gil de Paz, A., et al. 2012, A&A, 538, A8
Sánchez-Blázquez, P., Ocvirk, P., Gibson, B. K., Pérez, I., & Peletier, R. F. 2011, MNRAS, 415, 709
Sánchez-Blázquez, P., Peletier, R. F., Jiménez-Vicente, J., et al. 2006, MNRAS, 371, 703
Sanders, D. B., Soifer, B. T., Elias, J. H., Neugebauer, G., & Matthews, K. 1988, ApJ, 328, L35
Sarzi, M., Falcón-Barroso, J., Davies, R. L., et al. 2006, MNRAS, 366, 1151
Sarzi, M., Shields, J. C., Schawinski, K., et al. 2010, MNRAS, 402, 2187
Schawinski, K., Dowlin, N., Thomas, D., Urry, C. M., & Edmondson, E. 2010, ApJ, 714, L108
Schawinski, K., Koss, M., Berney, S., & Sartori, L. F. 2015, MNRAS, 451, 2517
Schawinski, K., Thomas, D., Sarzi, M., et al. 2007, MNRAS, 382, 1415
Schawinski, K., Urry, C. M., Simmons, B. D., et al. 2014, MNRAS, 440, 889
Schaye, J., Crain, R. A., Bower, R. G., et al. 2015, MNRAS, 446, 521
Schechter, P. L. & Gunn, J. E. 1979, ApJ, 229, 472
Schweizer, F. 1982, ApJ, 252, 455
Schweizer, F. & Seitzer, P. 1998, AJ, 116, 2206
Schweizer, F., Seitzer, P., Kelson, D. D., Villanueva, E. V., & Walth, G. L. 2013, ApJ, 773, 148

Scudder, J. M., Ellison, S. L., Torrey, P., Patton, D. R., & Mendel, J. T. 2012, MNRAS, 426, 549
Sellwood, J. A. & Spekkens, K. 2015, ArXiv e-prints [arXiv:1509.07120]
Serra, P., Oosterloo, T., Morganti, R., et al. 2012, MNRAS, 422, 1835
Singh, R., van de Ven, G., Jahnke, K., et al. 2013, A&A, 558, A43
Smethurst, R. J., Masters, K. L., Lintott, C. J., et al. 2018, MNRAS, 473, 2679
Somerville, R. S., Hopkins, P. F., Cox, T. J., Robertson, B. E., & Hernquist, L. 2008, MNRAS, 391, 481
Spekkens, K. & Sellwood, J. A. 2007, ApJ, 664, 204
Springel, V., Di Matteo, T., & Hernquist, L. 2005a, ApJ, 620, L79
Springel, V., White, S. D. M., Jenkins, A., et al. 2005b, Nature, 435, 629
Stern, J. & Laor, A. 2012, MNRAS, 426, 2703
Takeuchi, T. T., Buat, V., Heinis, S., et al. 2010, A&A, 514, A4
Taylor, E. N., Hopkins, A. M., Baldry, I. K., et al. 2011, MNRAS, 418, 1587
Teyssier, R., Chapon, D., & Bournaud, F. 2010, ApJ, 720, L149
Torrey, P., Cox, T. J., Kewley, L., & Hernquist, L. 2012, ApJ, 746, 108
Tsatsi, A., Lyubenova, M., van de Ven, G., et al. 2017, A&A, 606, A62
Ueda, J., Iono, D., Petitpas, G., et al. 2012, ApJ, 745, 65
Ueda, J., Iono, D., Yun, M. S., et al. 2014, ApJS, 214, 1
van de Sande, J., Bland-Hawthorn, J., Brough, S., et al. 2017, MNRAS, 472, 1272
Vazdekis, A., Sánchez-Blázquez, P., Falcón-Barroso, J., et al. 2010, MNRAS, 404, 1639
Veale, M., Ma, C.-P., Greene, J. E., et al. 2017, MNRAS, 471, 1428
Vogelsberger, M., Genel, S., Springel, V., et al. 2014a, Nature, 509, 177
Vogelsberger, M., Genel, S., Springel, V., et al. 2014b, MNRAS, 444, 1518
Wagner, S. J., Bender, R., & Moellenhoff, C. 1988, A&A, 195, L5
Walcher, C. J., Coelho, P. R. T., Gallazzi, A., et al. 2015, A&A, 582, A46
Wang, Z., Schweizer, F., & Scoville, N. Z. 1992, ApJ, 396, 510
Weigel, A. K., Schawinski, K., Caplar, N., et al. 2017, ApJ, 845, 145
Whitmore, B. C., Chandar, R., Schweizer, F., et al. 2010, AJ, 140, 75
Wild, V., Heckman, T., & Charlot, S. 2010, MNRAS, 405, 933
Wild, V., Rosales-Ortega, F., Falcón-Barroso, J., et al. 2014, A&A, 567, A132
Wong, K. C., Blanton, M. R., Burles, S. M., et al. 2011, ApJ, 728, 119
Woo, J.-H., Cho, H., Husemann, B., et al. 2014, MNRAS, 437, 32
Yamamura, I., Makiuti, S., Ikeda, N., et al. 2010, VizieR Online Data Catalog, 2298
Young, L. M., Bureau, M., Davis, T. A., et al. 2011, MNRAS, 414, 940